

Characteristics of fluid-induced resonances observed during microseismic monitoring

Jean Baptiste Tary,^{1,3} Mirko van der Baan¹, Bruce Sutherland¹ and David

W. Eaton²

Corresponding author: J. B. Tary, Department of Meteorology and Geophysics, University of Vienna, Austria. (jean-baptiste.tary@univie.ac.at)

¹Department of Physics, University of Alberta, Edmonton, Alberta, Canada.

²Department of Geoscience, University of Calgary, Calgary, Alberta, Canada.

³now at: Department of Meteorology and Geophysics, University of Vienna, Austria.

This article has been accepted for publication and undergone full peer review but has not been through the copyediting, typesetting, pagination and proofreading process, which may lead to differences between this version and the Version of Record. Please cite this article as doi: 10.1002/2014JB011263

Abstract.

Three groups of resonances are observed during a two-stage hydraulic experiment recorded by twelve 3-component geophones. The injected fluid is composed of a slurry of mostly water and proppant, plus some supercritical nitrogen. Resonance characteristics are estimated using an autoregressive model. Three resonance models are investigated: fluid-filled cracks, non-laminar fluid flow and repetitive events in terms of anticipated resonance frequencies, quality factors and amplitudes. The observed resonances are very stable and positively correlated with either the slurry flow or the nitrogen injection rate, which is in contradiction with the repetitive events and fluid-filled crack models, respectively. Resonances obtained by numerical simulations of an unstable jet agree with the main characteristics of most observed resonances. Our observations suggest that variations in resonance frequencies are mainly driven by variations in fluid flow, whereas quality factors are more sensitive to the fluid composition through variations in nitrogen injection rate. This study also suggests that resonance frequencies and quality factors can provide complementary information for real-time monitoring of fluid injection into reservoirs, for hydraulic stimulations, geothermal operations, carbon capture and storage or fluid movement during volcano eruptions.

1. Introduction

Fluid injection during hydraulic fracturing treatments generally produces numerous microseismic events, which are mainly caused by shear and tensile failure of the reservoir rocks [Baig and Urbancic, 2010; van der Baan et al., 2013]. The non-double-couple components in their focal mechanisms are often thought to be related to the presence of pressurized fluids within the host rocks or reservoir [Foulger and Long, 1984; Song and Toksöz, 2011; Guilhem et al., 2014]. Yet, reliable and confident interpretation of such focal mechanisms in terms of actual reservoir deformation is often hindered by multiple sources of uncertainties, which may introduce spurious non-double-couple components into the moment tensor solutions, including limited azimuthal coverage, errors in picking, event locations and/or velocity models [Godano et al., 2009; De Barros et al., 2013; Stierle et al., 2014], or unaccounted for velocity anisotropy [Šílený and Milev, 2008].

On the other hand, other observations including the spectral characteristics of microseismic events support the occurrence of tensile rupture, linked to the presence of fluids [Foulger et al., 2004; Eaton et al., 2014]. In this paper, we show that a spectral analysis of continuously recorded data, instead of relying on analysis of individual microseismic events, can reveal much about the fluid-flow patterns during hydraulic fracturing experiments. We will build on and extend the interpretational framework of Tary et al. [2014c] for analyzing spectral resonances.

Microseismic events are generally weak with moment magnitudes ranging between -4 and -1 [King, 2012; van der Baan et al., 2013], signal frequencies up to several hundreds Hz, and durations on the order of tenths of seconds [e.g., Warpinski, 2009; Eaton

et al., 2014]. As a way to control the efficiency of hydraulic fracturing, energy budget studies indicate that radiated seismic energy constitutes a negligible fraction of the input injected energy [Boroumand and Eaton, 2012; Maxwell *et al.*, 2009], which cannot be accounted for by fluid leak-off or friction within the well and the reservoir. Apart from near-instantaneous shear and tensile failure, other types of deformations must therefore take place during forced fluid injection such as aseismic deformation or slow slip [Chorney *et al.*, 2012]. Seismic signals associated with these kinds of deformation are expected to have long durations and emergent onsets, which make them difficult to detect by classical methods based on recognition of individual events via triggering and picking [Bame and Fehler, 1986]. Reported observations of such longstanding phenomena during fluid injection into reservoirs are therefore relatively rare [Bame and Fehler, 1986; Baria *et al.*, 1989; Ferrazzini *et al.*, 1990; Das and Zoback, 2013a; Eaton *et al.*, 2013; Tary *et al.*, 2014c; Caffagni and Eaton, 2014].

Various mechanisms are invoked to explain the generation of long-duration events, from the resonance of fluid-filled cracks [Bame and Fehler, 1986; Baria *et al.*, 1989; Ferrazzini *et al.*, 1990; Bohnhoff and Zoback, 2010] to a combination of high fluid pressure and favorable in-situ conditions [Das and Zoback, 2013b]. The low-frequency events described by Das and Zoback [2013a], called long-period long-duration events, have a lower frequency content than typical microseismic events (i.e., up to approximately 80 Hz) and longer durations on the order of tens of seconds. Das and Zoback [2013b] suggest that low-frequency events could even account for a substantial part of the missing energy in very low-permeability reservoir stimulation. Borehole geophones typically employed for microseismic monitoring have natural frequencies of 15 Hz, which is problematic for the

identification of low-frequency events and tremors that are recorded both in tectonic settings [Ide et al., 2007; Zhang et al., 2011] and at volcanoes [Chouet and Matoza, 2013] which have upper frequencies around 5-10 Hz. Low-frequency events actually correspond to the upper end of low-frequency phenomena including very-low-frequency and slow slip events [Ide et al., 2007] which cannot be recorded by current borehole networks.

The resonances reported in the present study are characterized by stable and narrow-band peaks, which would indicate the presence of a resonator or a semi-permanent and non-destructive physical process. These resonances seem analogous to harmonic tremors recorded at volcanoes [e.g., Hagerty et al., 2000] but at higher frequencies (\sim 15-60 Hz). The interpretation of resonance peaks is however difficult as they can arise from many causes on the receiver [Sun and McMechan, 1988; St-Onge and Eaton, 2011], path [Bonnefoy-Claudet et al., 2006] and source sides [Correig and Vila, 1993; Chouet et al., 1997]. Assuming that the resonances are introduced by source effects, three main mechanisms are generally proposed, namely resonance of fluid-filled cracks or conduits [Aki et al., 1977; Chouet, 1996; Bohnhoff and Zoback, 2010], fluid-flow in conduits [Julian, 1994; James et al., 2006; Rust et al., 2008; Chouet et al., 2010], and repetition of quasi-periodic events [Lees et al., 2004; Pettitt et al., 2009; Dmitrieva et al., 2013].

Interpretations of source-generated resonances relying only on their peak frequency often lead to multiple interpretations as entirely different mechanisms can produce similar resonance frequencies [e.g., Konstantinou and Schlindwein, 2002], and many parameters have similar effects on frequency within a single underlying causative mechanism [Chouet, 1986; Hellweg, 2000]. Two other characteristics of resonances, quality factors and amplitudes, are often disregarded even though they can bring information about the resonator

system or the filling fluid [Kumagai and Chouet, 2000]. Quality factors (Q-factor) are defined by the ratio central frequency f_0 to frequency bandwidth Δf at -3 dB, i.e., $Q = f_0/\Delta f$ [Selesnick, 2011]. Q-factors are a measure of resonance damping, e.g., a high Q-factor corresponds to narrow spectral peak and a long-duration waveform (Figure 1).

We here extend the analysis of resonances recorded during a microseismic experiment by Tary *et al.* [2014c], who show these are related to source effects at the perforation locations or inside the reservoir (case study 2). Tary *et al.* [2014c] suggest two possible models, fluid-filled cracks and non-laminar fluid-flow, as the physical cause of the main resonances. We also investigate a third possibility, namely repetitive events [e.g., Lees *et al.*, 2004]. It is however difficult to distinguish between these models based on frequency content alone. We show that the additional analysis of amplitudes and quality factors may help distinguish between the potential models. In the following we describe how Q-factors and amplitudes are obtained using an autoregressive (AR) model, and how they are useful for the interpretation of resonances in this microseismic experiment.

2. Calculation of quality factors

Except for their peak frequency, resonances are also characterized by their decay rate that is usually quantified by their quality factor Q [e.g., Aki, 1984]. Long-lasting resonances have high Q-factors while short-lived resonances have low Q-factors. AR coefficients, as they define the poles of the frequency response of a resonator, can also be used to obtain the Q-factors [Bellanger, 1981; Nakano *et al.*, 1998; Lesage *et al.*, 2002]. A resonant peak is represented by an AR filter of order 2 following

$$y_n = \epsilon_n - a_1 y_{n-1} - a_2 y_{n-2}, \quad (1)$$

where a_k are the filter coefficients, y_n a time series and ϵ_n is a white noise driving process.

The z -transform of the transfer function associated with this filter is given by

$$H(z) = \frac{1}{1 + a_1 z^{-1} + a_2 z^{-2}}. \quad (2)$$

Expression 2 has two conjugate poles P and \bar{P} when the discriminant of the characteristic function is negative [Bellanger, 1981] given by

$$P = -\frac{a_1}{2} + j\frac{1}{2}\sqrt{4a_2 - a_1^2} = re^{-j\theta} \quad (3)$$

where r and θ are the modulus and argument of P , respectively, \bar{P} is the complex conjugate of P , and $j = \sqrt{-1}$.

In addition, a characteristic frequency f_0 exists if $\cos \theta < (2r)/(1 + r^2)$ corresponding to the resonance frequency of the system. In this case, and for poles close to the unit circle ($r \approx 1$), the resonance frequency f_0 and quality factor Q can be found with [Bellanger, 1981; Lesage et al., 2002]

$$\begin{aligned} f_0 &\approx \frac{\theta}{2\pi\Delta t}, \\ Q &\approx \frac{\theta}{2(1-r)}, \end{aligned} \quad (4)$$

which is equivalent to $Q = f_0/\Delta f$ [Bellanger, 1981], and where Δt is the sampling interval.

For AR processes with orders higher than 2, we apply eqs. 1-3 for each conjugate pair of AR poles to obtain the corresponding resonance frequencies and Q-factors with eq. 4.

Complex frequencies are defined as $f - jg$, where f is the frequency and g is the growth rate given by $g = -f/2Q$. The clustering of AR poles in growth rate-frequency plots

also indicates if the AR order is suitable for the representation of the investigated part of the signal. Scattered points are associated with incoherent noise [Kumagai and Chouet, 2000].

We here estimate the AR coefficients using the Yule-Walker method [e.g., Kay and Marple, 1981; Monson, 1996], then calculate the resonance frequencies and quality factors from eq. 4 for a range of AR orders around the optimum value. We finally compute their mean and standard deviation to provide the final values of f_0 and Q and estimate the uncertainty on these measures. No Q-factors are shown when the resonance amplitude is too low to obtain reliable measurements. Amplitudes are estimated by taking the maximum amplitude in a narrow frequency band around the resonance frequency.

3. Application to a microseismic experiment

3.1. Experimental setup

The microseismic experiment is a 2-stage hydraulic stimulation targeting a tight-gas reservoir in the Cardium formation in western Canada (case history 2 in Tary *et al.* [2014c]). These stages were monitored by 12 geophones deployed in a vertical well located approximately 400 m from the injection (Figure 2). The fluid injection is taking place at the same depth as the receivers. The sensors are 15 Hz-geophones and the data are sampled at 4000 Hz.

The injected fluid constitutes mainly of a slurry of water, proppant, surfactant and chemical additives, and an energizer which is nitrogen (N_2) in our case. At the top of the well, the nitrogen is in the gaseous state and the proportions in volume are about 98% N_2 - 2% slurry, while downhole the nitrogen is in a supercritical state and the proportions are about 17% N_2 - 83% slurry. Downhole, the fluid-phase of the mixture slurry- N_2

has a viscosity between 0.025 and 0.15 Pa.s [Ribeiro and Sharma, 2012] and a density around 738 kg/m³. The average flow rates of the slurry on the surface are around 4 and 3.7 m³/min for the first and second stage, respectively, and about 5.3 and 5 m³/min downhole.

3.2. Observations

For both stages, a total of 190 microseismic events were detected and around one hundred of them were located. These events have magnitudes ranging from -4 to -3 and have frequencies mainly between 150 and 600 Hz. They define a SW-NE microseismic cloud including the injection well (Figure 2). Further information on this experiment and the geologic background of the area are given by Tary *et al.* [2014c].

3.2.1. Peak frequencies

The time-frequency analysis of both stages using the AR method of Tary *et al.* [2014b] is presented in Figure 3 together with the treatment curves. These time-frequency representations are very similar to those obtained using the short-time Fourier transform [Tary *et al.*, 2014c]. We determine the AR order based on spectral comparisons between AR and Fourier spectra [Tary *et al.*, 2014b] and the Akaike information criteria [Priestley, 1994]. The optimum AR order obtained for both stages is 100.

During the first stage, there are two main groups of resonances with frequencies at 17 Hz and 27 Hz (Figure 3). These two sets of resonances have harmonics at 35 and 51 Hz, and at 17-20, 32-36 and 50-53 Hz, respectively. These two groups of resonances are also observed during the second stage, together with a third group with a main frequency at 29 Hz, and one overtone at 58 Hz. The resonance at 60 Hz, present during both stages, corresponds to the electric current. The resonance family at 27 Hz and 29 Hz are positively correlated

with the slurry flow and the nitrogen injection rate, respectively. The resonance group at 17 Hz shows a more complex pattern, but seems more correlated to the nitrogen injection rate than the slurry flow.

For both stages, a time shift between the treatment curves and the time-frequency content is applied, +323 and +227 s for stage 1 and 2, respectively. This time shift may correspond to the time necessary for the fluid to reach the reservoir. The time to fill-up the well can be estimated using an average fluid flow and the volume of the well. The well has a volume of approximately 18.7 m³ and with an average fluid flow of 4 and 3.7 m³/min for the first and second stage, respectively, estimated time delays are 281 and 303 s. The observed delays are similar to this first-order estimation. Non-linear fluid flow or stress transfer between the injection front and the bottom of the well might explain the small discrepancy, as well as the presence of fluids inside the well prior to the injection or timing errors between the different clocks on the field, which are rarely GPS-synched.

3.2.2. Quality factors

As we are dealing with continuous data and not individual events, we are measuring peak frequencies, amplitude and Q-factors on successive, non-overlapping data segments. The Q-factor calculation depends on the number of AR coefficients and the size of the data window. We use a sliding window of 12.8 s, which is long-enough to include at least hundreds of cycles of the resonance with the lowest frequency (17 Hz). The AR order should be high enough to account for all spectral peaks because close-by spectral lines accounted for by a single AR pole will have artificially wide peaks and therefore lower Q-factors.

Quality factors are calculated from the AR poles computed for each data window using all selected AR orders (optimum AR order +/- 10 AR orders: 90-110). Final Q-factors corresponding to the main resonances are estimated by averaging the Q-factors obtained using the different AR orders. An example of a growth rate vs frequency plot is given in Figure 4 to show the clustering of AR poles. Their strong clustering for all resonances indicates that these AR orders are suitable for the calculation of the quality factors. A sketch of the frequencies, amplitude and quality factors corresponding to the three main resonance groups recorded by the deepest geophone are presented in Figures 5 and 6. In general, the resonance characteristics estimated for other geophones that recorded the resonances with enough amplitude show similar trends but with lower values.

The estimated Q-factors show a large variability with variances generally proportional to the estimated values. Variances also reflect lower signal-to-noise ratios for some resonances. For the first stage (Figure 5), the resonance at 51 Hz shows Q-factors mainly between approximately 400 and 700, which is higher than the other resonances with Q-factors mainly ranging between 40 and 300. Both overtones at 35 and 51 Hz display polarization azimuths similar to those of the background noise, possibly indicating noise contamination at these frequencies [Tary *et al.*, 2014c]. The large Q-values might then be partly arising from signal contamination as well as complex pattern in resonance frequencies (double-peaks).

3.2.3. Correlations between resonance characteristics and treatment curves

Interestingly, Q-factors suddenly increase between 1200 and 1400 s for the resonances at 17 and 51 Hz. Q-factors of the 17 Hz resonance are around 60 at the beginning of the fluid injection, shifting down to ~ 80 after the sudden increase. Compared to the

beginning of the stage, two small increases in Q-factors occur at around 1400 and 2150 s, both correlated to the slurry flow and the nitrogen injection rate. At the same time of the second Q-factor increase, the amplitude starts dropping progressively. This resonance almost disappears at around 2700 s, which corresponds to a decrease in nitrogen injection rate and an increase in slurry flow. In the case of the resonance at 35 Hz, the increase from 55 to 130 at 800 s is correlated with an increase in slurry flow and nitrogen rate. The progressive Q-factor increase up to around 330 corresponds to a decrease in resonance amplitude and a complex frequency pattern (Figure 3). Complex patterns in resonance frequencies seem to favor higher quality factors, as shown also by the Q-factors of the resonance at 51 Hz. Q-factors for the resonance at ~ 27 Hz are generally lower, ranging from 40 to 80. The step increase to 80 at 2100 s coincides with an increase in slurry flow and nitrogen injection rate, whereas the decrease at 2700 s is positively correlated with a decrease in nitrogen rate and anticorrelated with the slurry flow.

The resonance frequencies of the first group (17, 35 and 51 Hz) remain almost constant during the second stage (Figure 6), unlike corresponding Q-factors which show a large variability. For the first ~ 1500 s, Q-factors remain constant around 120 for the resonance at 51 Hz. Q-factors are progressively increasing from 50 to 120 and from 140 to 230 for the resonances at 29 and 35 Hz, respectively. Then, Q-factors increase for all resonances between 1900 and 2200 s, followed by a period with lower Q-values (2200-2550 s). Except for the resonance at 35 Hz, Q-factors are then rising again to $\sim 250-650$ and slowly decrease toward the end of the fluid injection. These changes in Q-factors seem to be correlated to changes in the nitrogen injection rate. The sudden increase in Q-factors at the end of the stage (4250-4450 s) for the resonances at 35 and 51 Hz could arise from

their complex pattern (Figure 3). In addition, for both stages, variations in Q-factor are generally positively correlated with variations in resonance amplitude. On the other hand, resonance characteristics seem unaffected by fluid pressure and proppant concentration. No Q-factors are calculated for the resonance at 16 Hz, which is following the slurry flow variations like the resonance at 27 Hz during the first stage, due to its low amplitude.

3.3. Interpretation

Causes of resonances recorded during hydraulic fracturing treatments can come from receiver, path or source effects. All these must be investigated prior to the resonances interpretation. For the present microseismic experiment, *Tary et al.* [2014c] study the potential causes of the observed resonances and conclude that source effects are the most likely cause. Measured Q-factors are also a superposition of the influences of path effects and source effects [*Eaton et al.*, 2014]. In the following we assume that changes in the resonance Q-factors reflect purely variations in their source-side causes as path effects do not correlate with treatment parameters. We further simplify our analysis by neglecting wave scattering effects, even though these could be important due to the complex geologic structure of the area [*Hart et al.*, 2007]. These assumptions could lead to an overestimation of the attenuation due to the source [*Jousset et al.*, 2004]. We then interpret the resonance characteristics considering the three postulated models for source resonances, after reviewing their effects on peak frequency, quality factor and amplitude.

3.3.1. Fluid-filled crack model

Resonance in fluid-filled cracks is due to the multiple reflections of a slow wave trapped inside the crack [*Chouet*, 1986]. This slow wave, also called Krauklis wave [*Korneev*, 2011], is a dispersive wave propagating along the crack walls. Its amplitudes vanish

exponentially from the crack walls [Ferrazzini et al., 1990]. The wavefield recorded by the sensors corresponds to the Krauklis wave diffraction at the crack tips [Frehner and Schmalholz, 2010].

The frequency response of fluid-filled cracks depends on the crack geometry (shape, dimensions), the excitation impulse, and the rock and fluid properties [Aki et al., 1977; Chouet, 1986]. Using the analytical derivation of the phase velocity of Krauklis waves of Korneev [2008] for an infinite layer embedded in an elastic solid, and considering a crack with closed, flat tips, the resonance frequency of the fluid-filled crack is given by [Korneev, 2008; Tary et al., 2014c]

$$f_{0,k} = \sqrt{\frac{h\mu\pi^3 k^3}{l^3\rho} (1 - \gamma^2)}, \quad k = 1, 2, 3, \dots, \quad (5)$$

where $f_{0,k}$ is the resonance frequency f_0 for mode k , μ is the shear modulus of the surrounding solid, ρ is the fluid density, γ is the ratio of S- to P-wave velocities of the solid (V_s/V_p), and h and l are the crack thickness and length, respectively. Eq. 5 corresponds to the “thick fracture” regime where the viscosity is neglected for cracks that are wide enough or for fluids with a low viscosity such as oil or water [Korneev, 2008; Frehner and Schmalholz, 2010].

Resonant frequency is then mainly dependent on the size and shape of the resonator and macro-properties of the fluid (density, viscosity, pressure) [Chouet, 1986; Korneev, 2008; Frehner and Schmalholz, 2010]. Aki [1984] and Kumagai and Chouet [2000] show that while Q-factors depend on the resonator geometry as well, they also respond to multi-phase contents (gas, solid particles), to the impedance contrast between the cavity and the surrounding rocks, and to thermal and viscous attenuation.

Quality factors calculated for fluid-filled crack models are decomposed in radiation losses

Q_r and intrinsic losses Q_i as [Aki, 1984]

$$Q^{-1} = Q_r^{-1} + Q_i^{-1}. \quad (6)$$

Radiation losses depend primarily on the acoustic impedance contrast between the fluid inside the crack and the rock [Aki, 1984; Kumagai and Chouet, 2000] and the geometry of the resonator. Q_r increases as the impedance increases and decreases as the ratio l/h increases. Intrinsic losses are mainly affected by the fluid content, such as the gas and solid particle contents [Kumagai and Chouet, 2000]. Q_i quickly decreases with increasing gas content until stabilization for gas content superior to 2 %, but it also depends on the bubble radius. Q_i also decreases with increasing number of solid particles, but it depends on the particle size as well. Q_i also includes thermal and viscous attenuation.

The relatively high Q-factors measured for some of the observed resonances could result from the presence of the supercritical nitrogen in the injected fluid. Q-factors are indeed very sensitive to the gas content of the resonator while the resonance frequencies are not [Kumagai and Chouet, 2000]. Large values for the Q-factor are thus generally associated with the presence of a gas phase.

If no Q-factor variations are observed, it could mean that the fluid properties and the dimensions of the fluid-filled fracture are stable or that an increase in length is compensated by an increase in thickness. When Q-factors are suddenly increasing (at 1000 s in the first stage or at 1950 s in the second stage), resonances are either slightly increasing or constant. In the case of the first stage, the nitrogen injection rate is also constant, which suggests that if additional gas is suddenly flowing inside the fracture it should come from

the reservoir. For the second stage, the sudden variations in Q-factors seem to be related to the nitrogen injection rate. When Q-factors are steadily decreasing (between 3000 and 4200 s in the second stage), it could indicate that some gas is progressively removed from the fluid-filled fracture. Very high Q-values generally correspond to spectral peaks with high amplitudes (at 1200 s in the first stage or at 1950 s in the second stage). This could result from an increase of the resonance amplitude by an increase of the impedance contrast between the fluid and the solid due to the gas.

While the fluid-filled crack model is consistent with some of the observations, such as the positive correlation between nitrogen injection rate increase (fluid density decrease) and resonance frequency increase (see eq. 5), resonance frequencies are also expected to decrease due to fracture expansion over time following the increases in slurry flow. For instance, the opposite is observed for the resonances at 27 and 16 Hz during the first and second stages, respectively, which shift toward higher frequencies every time the slurry flow increases. In the meantime, the corresponding Q-factors remain low (25-40) indicating that the fluid properties stay similar, or that its cause is not very sensitive to fluid properties. Alternatively, the resonances could be developing within pre-existing fracture networks that are essentially static during the treatment. Fluid flow models such as fluid flow in constricted conduits [*Julian, 1994; Rust et al., 2008*] or fluid-flow instabilities [*Hellweg, 2000; Rust et al., 2008*] could then explain some features of the observed resonances. In the following section, we describe how resonances could be generated by flow-induced vortices arising from Orr-Sommerfeld instabilities.

3.3.2. Fluid-flow model: Orr-Sommerfeld instabilities

When high-pressure fluids are injected into a fracture, the resulting jet may become unstable, breaking into vortices. The period of these vortices could be responsible for the observed low-frequency resonances. The large diversity of flow-induced vibrations are characterized by different frequency responses. Turbulent flow is associated with broadband excitation due to the different eddy sizes present in this type of flow [*Naudasher and Rockwell*, 1994]. Fluid flows impinging on an obstacle typically have a broadband frequency content as well, while the observed resonance frequencies have narrow-band spectral peaks. Even though various experimental settings are possible, we here consider a simple configuration where the fluid is flowing from the borehole into the reservoir through a circular perforation. The resulting fluid-flow instabilities are good candidates to explain our observations as they generate narrow-band resonance frequencies.

The onset of instability and frequency of vortices depends upon the flow speed through the orifice, the size of the orifice and the viscosity of the fluid. Although the equations used to predict the stability of a viscous jet flow were formulated by Orr and Sommerfeld over a century ago, only recently have sophisticated numerical methods been developed to solve them [e.g., *Drazin and Reid*, 1981]. Using these methods, we propose to assess the stability of the jet and to determine whether the observed resonances result from the growth and evolution vortices from an unstable jet.

Three methods will be employed. A so-called “shooting method” will integrate the equations assessing the stability of high velocity jets [*Sutherland and Peltier*, 1992]. For lower velocity jets, a so-called “Galerkin method” will decompose the stability equations into an algebraic matrix problem that incorporates the effects of viscosity and diffusivity

of the fluid [Sutherland and Peltier, 1994]. Finally, using a code that solves the fully nonlinear Navier Stokes equations, numerical simulations will be performed to examine the fully nonlinear evolution of the instability [Sutherland, 2006].

An example of the model output is shown in Fig. 7. The simulation was initialized with a jet having maximum speed $U = 200$ m/s and half-width $L = 0.005$ m, consistent with a $1 \text{ m}^3/\text{min}$ flow through a 0.01 m diameter perforation. These parameters should correspond approximately to the conditions at the beginning of the injection, when the resonances appear. Assuming the fluid has molecular viscosity of $\mu_m = 0.1$ Pa.s and density $\rho = 740 \text{ kg/m}^3$, the Reynolds number of this flow is $\text{Re} = 7400$. The Orr-Sommerfeld equations describing instabilities of this jet are solved using a Galerkin method and this structure is superimposed on the jet, allowing for 2 wavelengths of the instability to span the (horizontally periodic) domain. The Navier Stokes equations are then solved iteratively in time allowing the instability to grow (Fig. 7a) until the jet breaks into pairs of opposite signed vortices (Fig. 7b) and the same-signed vortices then merge (Fig. 7c).

The instability itself has a well-defined frequency associated with it. This can be computed by the linear stability analysis and it can be observed and measured in the numerical simulations. Given the high flow speed and small width of the jet simulation shown in Fig. 7, the frequency of the instability is orders of magnitude larger than 17 Hz. An order of magnitude of the expected frequency can be obtained using $\omega_0 \sim 0.4U/L$, with $\omega_0 = 2\pi f_0$, resulting in a frequency of ~ 2550 Hz in our case.

The stability analysis is well-suited to exploring sensitivity to initial conditions. Assuming a circular opening, the equations for the Reynolds number and the resonance

frequency can be re-written to emphasize their dependence on the opening half-width L

as

$$\begin{aligned} Re &= \frac{\rho UL}{\mu_m} = \frac{\rho Q_f}{\mu_m \pi L}, \\ f_0 &= \frac{0.4U}{2\pi L} = \frac{0.4Q_f}{2\pi^2 L^3}, \end{aligned} \quad (7)$$

where Q_f is the fluid flow in m^3/s . However, oil companies often use a cluster of a few perforations instead of a single one in order to increase the fluid flow inside the reservoir.

The jets coming from the different perforations will eventually merge in a single one with an effective size corresponding to the sum of the individual perforations. For an opening radius of 0.025 m corresponding to five perforations instead of 0.005 m for one perforation, the frequency predicted by this model is around 20 Hz, which is in the same range as the observed resonances.

The size of the eddies involved in the jet depends also on the size of the opening. The wavenumber is given by $k_0 \sim 0.9/L$, and the wavelength, corresponding approximately to the distance inter-eddies, by $\lambda_0 = 2\pi L/0.9$. The eddies radius corresponds to about a quarter of wavelength, which is around 0.04 m for an opening half-width of 0.025 m.

For this model, we anticipate the quality factors to reflect the pressure variations at the fluid-solid interface, controlled by the impedance contrast, and the life-time of the eddies. Eddy destruction is a complex process caused by any flow disturbances that promote turbulent flow. Irregularities can be due to multiple factors such as viscosity, conditions at the opening, 3-D turbulence effects, or irregular surfaces. Quality factors will then be influenced by the system geometry as well as the fluid composition. The fact that

numerous factors affect the timescale for the existence of eddies could also explain the relative instability of measured quality factors as shown in Figures 5 and 6.

3.3.3. Repetitive events

Resonances can be introduced by periodic, repetitive events similarly to a finite Dirac comb [Lees *et al.*, 2004; Hotovec *et al.*, 2013]. The time series, containing N events spaced by a time interval τ , create spectral peaks at

$$f_{0,k} = k/\tau, \quad k = 1, 2, 3, \dots, \quad (8)$$

convolved with a sinc function due to the finite length of the data [e.g., Smylie, 2013] and the event spectra [Dmitrieva *et al.*, 2013]. The width of the spectral peaks is then affected by the duration of the individual repetitive events ($\sim N\tau$). Irregularities in the periodic repetition of these events may also widen the spectral lines as well as disturb their shape in time-frequency representations, or even make them disappear for small irregular perturbations in event timing in the order of 15-20 % [Lees *et al.*, 2004].

Interpretations in terms of quality factors are then difficult for this model, as their cause may be a combination of waveform attenuation, period irregularities and spectral smearing. The amplitude of the spectral peaks depends on the number of events and their amplitudes.

For the following calculation we consider a longitudinal fracture propagation characterized by successive ruptures on a single plane. Using an average fracture propagation speed, the events frequency $f_{0,1}$, and an average event radius r_e , a moment magnitude can be estimated. For example, using a low fracture propagation speed of 0.1 m/s [Detournay and Garagash, 2003] consistent with the length of the long axis of the microseismic cloud,

an event frequency of 17 events/s, and assuming a 1-D fracture propagation by one event radii at a time, the individual events have a radii of about 0.006 m. The seismic moment M_o for a rupture on a circular crack is

$$M_o = \mu S D = \mu \pi r_e^2 h, \quad (9)$$

where S is the crack surface area, D the average coseismic displacement corresponding to the opening h for a tensile rupture. Considering a fracture opening of 0.0001 m for a 0.012 m-long fracture [Vermilye and Scholz, 1995] and a shear modulus of 17.4 GPa [Tary et al., 2014c], the seismic moment is approximately 200 N.m. The corresponding moment magnitude [Lee and Stewart, 1981], given by

$$M_w = \frac{2}{3} \log_{10} (M_o) - 6, \quad (10)$$

is $M_w \sim -4.5$. During the first stage, the resonance at 17 Hz lasts for approximately 42 min. Adding the seismic moments of 17 events/s for this period would correspond to a cumulative magnitude of around -1.4 .

Repetitive events could be of different origins. They could be directly linked to the fluid movements within the reservoir, e.g., to the intermittent opening and closing of fractures [Foulger and Long, 1984; Eaton et al., 2014], choked flow [Lees et al., 2004] or periodic turbulent slugs [Hellweg, 2000]. On the other hand, multiplets are repetitive events with sufficiently high waveform correlation to allow for analysis including double-difference event locations [Got et al., 1994; Castellanos and van der Baan, 2013]. Multiplet groups include both seismic repeaters [e.g., Chen et al., 2013] and successive events whose physical separation is much less than the seismic wave path length and whose focal mechanisms are

very similar. Such successive events might include a progressive rupture sequence along a fault or fracture. For the same area to rupture consecutively in short time intervals, it means that this patch is being cyclically re-stressed locally by another process, such as aseismic slip [Bouchon *et al.*, 2011], tectonic or coseismic stresses [Nadeau *et al.*, 1995], or over-pressurized fluids [Daniel *et al.*, 2011].

Geologic evidence exists for successive ruptures by a characteristic event on the same fracture plane, such as the plume-like features shown in Davis *et al.* [2011] and Bahat and Engelder [1984]. Sequences of impulsive events in volcanoes seem to last between one to several minutes [Lees *et al.*, 2004; Hotovec *et al.*, 2013], whereas the observed resonances have stable frequencies for durations of a few tens of minutes. The high sensitivity to period irregularities of spectral lines and the unstable character of fracture propagation seem contradictory. However, flow-related impulsive events are still possible if the flow conditions remain the same.

4. Discussion

In this paper, we use a time-varying autoregressive method applying an AR model on successive, overlapping windows, to obtain the time-frequency representation of the continuous recordings [Tary *et al.*, 2014b]. Other time-frequency transforms such as the short-time Fourier, continuous wavelet and S transforms also show the existence of the resonance frequencies [Tary and van der Baan, 2012]. No attempt was made to obtain independent estimates of the Q-factor using these alternative transforms, although a first look did reveal variations in the frequency spread of the resonances with time, indicating temporal variations in attenuation factors. Different time-frequency transforms emphasize different features in data [Tary *et al.*, 2014a]. The consistent presence of the resonance

frequencies independent of the applied time-frequency transform thus provides confidence in their existence.

AR methods provide an efficient way to both analyze the time-varying variations of resonances using time-frequency representations and measure their damping through their Q-factors. However, Q-factor estimation depends critically on the AR order and to a lesser extent on the window size of the signal. Uncertainties associated with this measure are then a very important item to take into account prior to any interpretation.

Quality factors associated with each resonance could help discriminating between different potential causes in some cases. Q-factors have been used to determine the characteristics of magmatic and hydrothermal fluids because of their high sensitivity to the fluid properties (e.g., density, sound velocity, gas content, presence of solid particles) as well as the shape of the resonator [Nakano *et al.*, 1998; Kumagai and Chouet, 2000]. For example, an increase in fracture length can be counterbalanced by an increase in fracture width, but the Q-factor would be different.

Contrary to single measurements performed on long-period events in volcano seismology [Nakano *et al.*, 1998; Kumagai *et al.*, 2002; Lesage *et al.*, 2002], we here measure quality factors for continuous resonances providing multiple measurements for the same spectral peak over time. The resulting curves show that, like frequency or amplitude estimates, Q-factors are time-dependent. They display both rapid oscillations (i.e., at the time scale of a few window sizes) and long-duration variations over time. One question is to know whether these variations reflect changes in the physical system or if they are due to the measurement method.

Rapid oscillations may be partly due to measurement instabilities as the parameters estimation for the AR process (i.e., AR order, window size) is performed for the complete time series and not locally. Uncertainties could also arise from data contamination by coherent noise or transient events in the frequency band of interest. On the other hand, large variations are systematically associated with variations in resonance amplitudes and frequency, as well as changes in treatment conditions. Therefore, they are likely linked to physical changes occurring during the fluid injection.

The potential generation of the observed resonances by the pumping equipment is explored by *Tary et al.* [2014c]. This explanation is unlikely owing to 1) the observation of the highest resonance frequencies amplitudes on the two deepest geophones; 2) the upward move-out of some individual wavepackets and the first appearance of the resonance on the deepest sensors; 3) the long time delay between the beginning of the injection operations and the onset of the resonances compared to direct wave propagation and resulting travel-times between the geophones and the well-head; 4) polarization measurements pointing to the perforations' location and incidence angles that are nearly horizontal or pointing downwards.

The fluid-flow model developed here can explain the observed narrow-band spectral peaks. We use a conservative approach by examining the numerical simulations for a simple model, i.e., the fluid flow of an homogeneous fluid through a circular perforation. Other fluid-flow models could also be appropriate but they require more specific configurations, such as vortex shedding which requires the presence of an obstacle in the flow [*Naudasher and Rockwell*, 1994; *Hellweg*, 2000]. On the other hand, pressure variations

due to fluid flow instabilities could simply provide the excitation mechanism for another resonator, such as a fluid-filled crack.

In brief, during both stages, resonance frequencies are either correlated to variations in slurry flow (27 and 16 Hz plus harmonics) or the nitrogen injection rate (17 Hz and 29 Hz plus harmonics). On the other hand, quality factors seem more correlated with variations in nitrogen injection rate whatever the resonance. For instance, the resonance frequency at 27 Hz is clearly following slurry flow variations whereas their quality factors are correlated with the nitrogen rate. In this case, we propose that the presence of this resonance frequency could be explained by fluid flow instabilities while quality factors would respond predominantly to changes in fluid composition. In addition, most fluid-flow models show a positive correlation between fluid-flow velocity and resonance frequency [Hellweg, 2000; Rust *et al.*, 2008], as observed.

Noticeably, the disappearance of the resonance at 17 Hz during the first stage is correlated both to a decrease in nitrogen injection rate and an increase in slurry flow. The high Reynolds number associated with the fluid-flow in this microseismic experiment implies that even moderate viscosity and density variations have limited impacts on the resonance frequencies. The small decrease in supercritical nitrogen injection rate (-8%) seems then insufficient to explain the disappearance of this resonance, even though properties of supercritical fluids can undergo large variations in response to relatively small perturbations [Carlès, 2010].

Considering a fluid-filled crack model, it would require either the collapse of the resonating fracture or, assuming a highly damped resonator, a sudden halt of the trigger mechanism inside the fracture. A fracture collapse is very unlikely due to the increase

in slurry flow. A sudden stop of the sustaining mechanism is a plausible explanation for fluid-flow models [Rust *et al.*, 2008] but also for resonances excited in a fluid-filled crack, although the high Q-factors observed would indicate a lightly-damped resonator. A change in fluid-flow regime to turbulent flow for example, could extinguish the resonance frequencies. Resonance characteristics are also strongly affected by perforations and fractures geometry.

Important question remains, such as what are the effects of proppant concentration or multi-phase supercritical fluids (i.e., solid particles, bubbles, non-Newtonian behavior) on resonances and quality factors? Why one resonance frequency is correlated to the slurry flow and another to the nitrogen injection rate while their quality factors are correlated to the nitrogen injection rate? This could indicate that quality factors indeed reflect the fluid composition and that different fluid-flow instabilities generate the two groups of resonances.

At volcanoes, long-period signals and harmonic tremors have frequencies in the range 0.5-10 Hz [Chouet, 1996], which is slightly lower than our observations. Fluid flow velocities are however one to two orders of magnitude smaller in volcanoes compared to hydraulic fracturing treatments. To obtain high Reynolds numbers necessary for the development of Orr-Sommerfeld instabilities in the frequency range of volcanic tremors and long-period events, it would require large conduits and/or low-viscosity fluids such as very low-viscosity magma or gas [Hellweg, 2000]. The most plausible scenario occurs if some fluid-filled cavities in the upper part of the volcano (e.g., in the damage zone surrounding the conduit or in blocked portions of the upper conduit) are suddenly heated up by magma, generating steam or overpressured fluids, which then bursts out of the cavity

through thin fractures. The large overpressure cause high flow velocities and could produce jet instabilities. Alternatively, edices and vortices could be created by interaction of flowing magma fluids with kinks and undulations in the volcano conduit, possibly causing low-frequency resonances [*Benson et al.*, 2008].

In order to explain high Q-factors in the order of several hundred, fluid-filled crack models would require a complex combination of several parameters (e.g., presence of gas, small bubbles or particles sizes) [*Kumagai and Chouet*, 2000]. These conditions could be met during hydraulic experiments using proppant, foam or energized fluids, even though the behavior of supercritical fluids in this case remains speculative. On the other hand, Q-factors of resonances due to Orr-Sommerfeld instabilities are mainly linked to their excitation i.e., the repetition of vortices of similar size. This model provides then an intuitive explanation for long-lasting resonances and high Q-factors. By adjusting fluid velocity U and fracture half-width L , the jet instabilities model may therefore also be able to reproduce the main resonance characteristics of low-frequency, harmonic signals occurring at volcanoes. This may also indicates that fluid dynamics, and the interaction between magma, the conduit and possibly the damage zone surrounding the conduit, may have a larger influence on the creation of low-frequency tremors [*Julian*, 1994; *Benson et al.*, 2008] than previously postulated.

5. Conclusion

Resonance frequencies, as well as their amplitudes and quality factors, are estimated for two stages of a hydraulic experiment using an AR model. We observe three main groups of resonances displaying very stable characteristics mainly correlated with the slurry flow and the nitrogen injection rate. The high correlation between slurry flow, nitrogen injection

rate, resonance frequency and quality factors suggests that fluid flow models are more likely to explain the generation of most of the observed resonances. Depending on the group of resonances, different fluid flow models could be at play. With the exception of the group of resonances at 17 Hz mostly unaffected by pumping rates, suggesting that the resonance of a fluid-filled crack of stable properties could potentially explain this set of resonances.

Resonance frequencies seem driven by variations in fluid flow velocities while quality factors seem primarily connected to the fluid composition through the proportion in supercritical nitrogen. Although the present analysis is semi-quantitative, it shows promising results concerning the use of quality factors for real-time monitoring of the fluid state during hydraulic stimulation for fracturing, geothermal operations, and carbon capture and storage.

Acknowledgments. The authors would like to thank the sponsors of the Microseismic Industry consortium for financial support, and an anonymous company for permission to show and use their data. Data shown in the figures are owned by a private company and currently proprietary. Codes to compute quality factors and growth rates are modified from the Seismo_volcanalysis software provided as supplementary material of Lesage [2006]. We thank two anonymous reviewers for their useful comments which improved the quality of the original manuscript.

References

Aki, K., Fehler, M., and S. Das (1977), Source mechanism of volcanic tremors: fluid-driven crack model and their application to the 1963 Kilauea eruption, *Journal of Volcanology*

and *Geothermal Research*, 2(3), 259–287.

Aki, K. (1984), Evidence for Magma Intrusion During the Mammoth Lakes Earthquakes of May 1980 and Implications of the Absence of Volcanic (Harmonic) Tremor, *Journal of Geophysical Research*, 89(B9), 7689–7686, doi:10.1029/JB089iB09p07689.

Bahat, D., and T. Engelder (1984), Surface morphology on cross-fold joints of the Appalachian Plateau, New York and Pennsylvania, *Tectonophysics*, 104(3–4), 299–313.

Baig, A., and T. Urbancic (2010), Microseismic moment tensors: A path to understanding frac growth, *The Leading Edge*, 29(3), 320–324.

Bame, D., and M. Fehler (1986), Observations of long period earthquakes accompanying hydraulic fracturing, *Geophysical Research Letters*, 13(1), 149–152, doi:10.1029/GL013i002p00149.

Baria, R., Green, A. S. P., and R. H. Jones (1989), Anomalous seismic events observed at the CSM HDR project, U.K., *International Journal of Rock Mechanics and Mining Sciences & Geomechanics Abstracts*, 26(3–4), 257–269.

Bellanger, M. (1981), *Traitement numérique du signal*, Masson, Paris.

Bohnhoff, M., and M. D. Zoback (2010), Oscillation of fluid-filled cracks triggered by degassing of CO₂ due to leakage along wellbores, *Journal of Geophysical Research*, 115, B11305, doi:10.1029/2010JB000848.

Benson, P. M., Vinciguerra, S., Meredith, P. G., and R. P. Young, (2008), Laboratory Simulation of Volcano Seismicity, *Science*, 322, 249–252, doi:10.1126/science.1161927.

Bonnefoy–Claudet, S., Cotton, F., and P.–Y. Bard (2006), The nature of noise wavefield and its applications for site effects studies: a literature review, *Earth–Sci. Rev.*, 79(3–4), 205–227, doi:10.1016/j.earscirev.2006.07.004.

Boroumand, N., and D. W. Eaton (2012), Comparing energy calculations - hydraulic fracturing and microseismic monitoring, paper presented at CSEG GeoConvention, Calgary.

Bouchon, M., Karabulut, H., Aktar, M., Özalaybey, S., Schmittbuhl, J., and M.-P. Bouin (2011), Extended Nucleation of the 1999 M_w 7.6 Izmit Earthquake, *Science*, *331*, 877–880, doi:10.1126/science.1197341.

Caffagni, E. C., and D. W. Eaton (2014), Reprocessing and Characterization of Long-duration Tremor Signals from a Hydraulic-fracture Treatment in Western Canada, paper presented at the 76th EAGE Conference and Exhibition, Amsterdam.

Carlès, P. (2010), A brief review of the thermophysical properties of supercritical fluids, *Journal of Supercritical Fluids*, *53*(1-3), 2–11, doi:10.1016/j.sup?u.2010.02.017.

Castellanos, F., and M. van der Baan (2013), Microseismic event locations using the double-difference algorithm, *CSEG Recorder*, *38*(3), 26–37.

Chen, K. H., Bürgmann, R., and R. M. Nadeau (2013), Do earthquakes talk to each other? Triggering and interaction of repeating sequences at Parkfield, *Journal of Geophysical Research*, *118*, 165–182, doi:10.1029/2012JB009486.

Chorney, D., P. Jain, M. Grob, and M. van der Baan (2012), Geomechanical modeling of rock fracturing and associated microseismicity, *The Leading Edge*, *31*(11), 1348–1354, doi:10.1190/tle31111348.1.

Chouet, B. (1986), Dynamics of a fluid-driven crack in three dimensions by the finite difference method, *Journal of Geophysical Research*, *91*(B14), 13967–13992, doi:10.1029/JB091iB14p13967.

Chouet, B. A. (1996), Long-period volcano seismicity: its source and use in eruption forecasting, *Nature*, *380*, 309–316.

Chouet, B. A., Dawson, P. B., James, M. R., and S. J. Lane (2010), Seismic source mechanism of degassing bursts at Kilauea Volcano, Hawaii: Results from waveform inversion in the 10–50 s band, *Journal of Geophysical Research*, *115*(B9), B09311, doi:10.1029/2009JB006661.

Chouet, B. A., and R. S. Matoza (2013), A multi-decadal view of seismic methods for detecting precursors of magma movement and eruption, *Journal of Volcanology and Geothermal Research*, *252*, 108–175, doi:10.1016/j.jvolgeores.2012.11.013.

Chouet, B., Saccorotti, G., Martini, M., Dawson, P., De Luca, G., Milana, G., and R. Scarpa (1997), Source and path effects in the wave fields of tremor and explosions at Stromboli Volcano, Italy, *Journal of Geophysical Research*, *102*(B7), 15129–15150, doi:doi:10.1029/97JB00953.

Cipolla, C., Maxwell, S., Mack, M., and R. Downie (2011), A Practical Guide to Interpreting Microseismic Measurements, *SPE international conference*, *SPE 144067*.

Correig, A. M., and J. Vila (1993), On the frequency contents of local events: source or path effect?, *Geophysical Journal International*, *115*(3), 863–877, doi:10.1111/j.1365-246X.1993.tb01498.x.

Daniel, G., Prono, E., Renard, F., Thouvenot, F., Hainzl, S., Marsan, D., Helmstetter, A., Traversa, P., Got, J. L., Jenatton, L., and R. Guiguet (2011), Changes in effective stress during the 2003–2004 Ubaye seismic swarm, France, *Journal of Geophysical Research*, *116*, B01309, doi:10.1029/2010JB007551.

Das, I., and M. D. Zoback (2013a), Long-period, long-duration seismic events during hydraulic stimulation of shale and tight-gas reservoirs – Part 1: Waveform characteristics, *Geophysics*, *78*(6), KS107–KS118, doi:10.1190/GEO2013-0164.1.

Das, I., and M. D. Zoback (2013b), Long-period, long-duration seismic events during hydraulic stimulation of shale and tight-gas reservoirs – Part 2: Location and mechanisms, *Geophysics*, 78(6), KS97–KS105, doi:10.1190/GEO2013-0165.1.

Davis, G. H., Reynolds, S. J., and C. F. Kluth (2011), *Structural Geology of Rocks and Regions*, 3rd Ed., Wiley, Hoboken, NJ.

De Barros, L., Lokmer, I., and C. J. Bean (2013), Origin of spurious single forces in the source mechanism of volcanic seismicity, *Journal of Volcanology and Geothermal Research*, 262, 1–6, doi:10.1016/j.jvolgeores.2013.06.006.

Detournay, E., and D. I. Garagash (2003), The near-tip region of a fluid-driven fracture propagating in a permeable elastic solid, *Journal of Fluid Mechanics*, 494, 1–32, doi:10.1017/S0022112003005275.

Dmitrieva, K., Hotovec-Ellis, A. J., Prejean, S. and E. M. Dunham (2013), Frictional-faulting model for harmonic tremor before Redoubt Volcano eruptions, *Nature Geoscience*, 6(8), 652–656, doi:10.1038/ngeo1879.

Drazin, P. G., and W. H. Reid (1981), *Hydrodynamic Stability*, Cambridge University Press, Cambridge.

Eaton D. W., Van der Baan, M., Birkelo, B. and J.-B. Tary (2014), Scaling relations and spectral characteristics of tensile microseisms: evidence for opening/closing cracks during hydraulic fracturing, *Geophysical Journal International*, 196(3), 1844–1857, doi:10.1093/gji/ggt498.

Eaton, D., van der Baan, M., Tary, J. B., Birkelo, B., Spriggs, N., Cutten, S., and K. Pike (2013), Broadband microseismic observations from a Montney hydraulic fracture treatment, northeastern B.C., Canada, *CSEG Recorder*, 38(3), 44–53.

Ferrazzini, V., Chouet, B., Fehler, M., and K. Aki (1990), Quantitative analysis of long-period events recorded during hydrofracture experiments at Fenton Hill, New Mexico, *Journal of Geophysical Research*, *95*(B13), 21871–21884, doi:10.1029/JB095iB13p21871.

Foulger, G. R., Julian, B. R., Hill, D. P., Pitt, A. M., Malin, P. E., and E. Shalev (2004), Non-double-couple microearthquakes at Long Valley caldera, California, provide evidence for hydraulic fracturing, *Journal of Volcanology and Geothermal Research*, *132*, 45–71, doi:10.1016/S0377-0273(03)00420-7.

Foulger, G. R. and R. E. Long (1984), Anomalous focal mechanisms: tensile crack formation on an accreting plate boundary, *Nature*, *310*, 43–45, doi:10.1038/310043a0.

Frehner, M., and S. M. Schmalholz (2010), Finite-element simulations of Stoneley guided-waves reflection and scattering at the tips of fluid-filled fractures, *Geophysics*, *75*(2), T23–T36.

Godano, M., Regnier, M., Deschamps, A., Bardainne, T., and E. Gaucher (2009), Focal Mechanisms from Sparse Observations by Nonlinear Inversion of Amplitudes: Method and Tests on Synthetic and Real Data, *Bulletin of the Seismological Society of America*, *99*(4), 2243–2264, doi:10.1785/0120080210.

Got, J.-L., Fréchet, J., and F. W. Klein (1994), Deep fault plane geometry inferred from multiplet relative relocation beneath the south flank of Kilauea, *Journal of Geophysical Research*, *99*(B8), 15375–15386, doi:10.1029/94JB00577.

Guilhem, A., Hutchings, L., Dreger, D. S., and L. R. Johnson (2014), Moment tensor inversions of $M \sim 3$ earthquakes in the Geysers geothermal fields, California, *Journal of Geophysical Research*, *119*, 2121–2137, doi:10.1002/2013JB010271.

Hagerty, M. T., Schwartz, S. Y., Garcés, M. A., and M. Protti (2000), Analysis of seismic and acoustic observations at Arenal Volcano, Costa Rica, 1995–1997, *Journal of Volcanology and Geothermal Research*, *101*(1–2), 27–65, doi:10.1016/S0377-0273(00)00162-

1.

Hart, B. S., B. L. Varban, K. J. Marfurt, and A. G. Plint (2007), Blind thrusts and fault-related folds in the Upper Cretaceous Alberta Group, deep basin, west-central Alberta: implications for fractured reservoirs, *Bulletin of Canadian Petroleum Geology*, *55*(2), 125–137, doi:10.2113/gscpgbull.55.2.125.

Hellweg, M. (2000), Physical models for the source of Lascar's harmonic tremor, *Journal of Volcanology and Geothermal Research*, *101*(1-2), 183–198, doi:10.1016/S0377-0273(00)00163-3.

Hotovec, A. J., Prejean, S. G., Vidale, J. E., and J. Gomberg (2013), Strongly gliding harmonic tremor during the 2009 eruption of Redoubt Volcano, *Journal of Volcanology and Geothermal Research*, *259*, 89–99, doi:10.1016/j.jvolgeores.2012.01.001.

Ide, S., Beroza, G. C., Shelly, D. R., and T. Uchide (2007), A scaling law for slow earthquakes, *Nature*, *447*, 76–79, doi:10.1038/nature05780.

James, M. R., Lane, S. J., and B. A. Chouet (2006), Gas slug ascent through changes in conduit diameter: Laboratory insights into a volcano-seismic source process in low-viscosity magmas, *Journal of Geophysical Research*, *111*(B5), B05201, doi:10.1029/2005JB003718.

Jousset, P., Neuberg, J., and A. Jolly (2004), Modelling low-frequency volcanic earthquakes in a viscoelastic medium with topography, *Geophysical Journal International*, *159*(2), 776–802, doi:10.1111/j.1365-246X.2004.02411.x.

Julian, B. R. (1994), Volcanic tremor: Nonlinear excitation by fluid flow, *Journal of Geophysical Research*, 99(B6), 11859–11877.

Kay, S., and S. Marple (1981), Spectrum Analysis-A modern perspective, *Proceedings of the IEEE*, 69(11), 1380–1419, doi:10.1109/PROC.1981.12184.

King, G. E. (2012), Hydraulic Fracturing 101: What Every Representative, Environmentalist, Regulator, Reporter, Investor, University Researcher, Neighbor and Engineer Should Know About Estimating Frac Risk and Improving Frac Performance in Unconventional Gas and Oil Wells, *SPE Hydraulic Fracturing Technology Conference*, SPE 152596, The Woodlands, TX.

Konstantinou, K. I., and V. Schlindwein (2002), Nature, wavefield properties and source mechanism of volcanic tremor: a review, *Journal of Volcanology and Geothermal Research*, 119, 161–187, doi:10.1016/S0377-0273(02)00311-6.

Korneev, V. (2008), Slow waves in fractures filled with viscous fluid, *Geophysics*, 73(1), N1–N7, doi:10.1190/1.2802174.

Korneev, V. (2011), Krauklis wave in a stack of alternating fluid-elastic layers, *Geophysics*, 76(6), N47–N53, doi:10.1190/geo2011-0086.1.

Kumagai, H., and B. Chouet (2000), Acoustic properties of a crack containing magmatic or hydrothermal fluids, *Journal of Geophysical Research*, 105(B11), 25493–25512, doi:10.1029/2000JB900273.

Kumagai, H., Chouet, B. A., and M. Nakano (2002), Temporal evolution of a hydrothermal system in Kusatsu-Shirane Volcano, Japan, inferred from the complex frequencies of long-period events, *Journal of Geophysical Research*, 107(B10), ESE 9-1–ESE 9-10, doi:10.1029/2001JB000653.

Lee, W. H., and S. W. Stewart (1981), *Principles and applications of micro-earthquake network*, Adv. Geophys., Supplement 2, Academic Press, New York.

Lees, J. M., Gordeev, E. I., and M. Ripepe, 2004, Explosions and periodic tremor at Karymsky volcano, Kamchatka, Russia, *Geophysical Journal International*, 158(3), 1151–1167, doi:10.1111/j.1365-246X.2004.02239.x.

Lesage, P., 2006, Interactive Matlab software for the analysis of seismic volcanic signals, *Computers & Geosciences*, 35(10), 2137–2144, doi:10.1016/j.cageo.2009.01.010.

Lesage, P., 2008, Automatic estimation of optimal autoregressive filters for the analysis of volcanic seismic activity, *Nat. Hazards Earth Syst. Sci.*, 8, 369–376, doi:10.5194/nhess-8-369-2008.

Lesage, P., Glangaud, F., and J. Mars (2002), Applications of autoregressive models and time–frequency analysis to the study of volcanic tremor and long–period events, *Journal of Volcanology and Geothermal Research*, 114(3-4), 391–417, doi:10.1016/S0377-0273(01)00298-0.

Maxwell, S. C., Shemeta, J., Campbell, E., and D. Quirk (2009), Microseismic Deformation Rate Monitoring, paper presented at EAGE Passive Seismic Workshop, Limassol, Cyprus.

Monson, H. (1996), *Statistical Digital Signal Processing and Modeling*, John Wiley & Sons, Hoboken.

Nadeau, R. M., Foxall, W., and T. V. McEvilly (1995), Clustering and Periodic Recurrence of Microearthquakes on the San Andreas Fault at Parkfield, California, *Science*, 267, 503–507, doi:10.2307/2886200.

Nakano, M., Kumagai, H., Kumazawa, M., Yamaoka, K., and B. A. Chouet (1994), The excitation and characteristic frequency of the long-period volcanic event: An approach based on an inhomogeneous autoregressive model of a linear dynamic system, *Journal of Geophysical Research*, *103*(B5), 10031–10046, doi:10.1029/98JB00387.

Naudasher, E., and D. Rockwell (1994), *Flow induced vibrations – An engineering guide*, A. A. Balkema, Rotterdam.

Pettitt, W., Reyes-montes, J., Hemmings, B., Hughes, E., and R. P. Young (2009), Using Continuous Microseismic Records for Hydrofracture Diagnostics and Mechanics, paper presented at SEG 79th Annual International Meeting, Houston.

Priestley, M. B. (1994), *Spectral Analysis and Time Series*, Academic Press, London.

Ribeiro, L. H., and M. M. Sharma (2012), Multiphase Fluid-Loss Properties and Return Permeability of Energized Fracturing Fluids, *SPE Productions & Operations*, *27*(3), 265–277, SPE-139622-PA, doi:10.2118/139622-PA.

Rust, A. C., Balmforth, N. J., and S. Mandre (2008), The feasibility of generating low-frequency volcano seismicity by flow through a deformable channel, *Geological Society, London, Special Publications*, *307*, 45–56, doi:10.1144/SP307.4.

Selesnick, I. W. (2011), Resonance-based signal decomposition: A new sparsity-enabled signal analysis method, *Signal Processing*, *91*, 2793–2809, doi:10.1016/j.sigpro.2010.10.018.

Šílený, J. and A. Milev (2008), Source mechanism of mining induced seismic events – Resolution of double couple and non double couple models, *Tectonophysics*, *456*, 3–15, doi:10.1016/j.tecto.2006.09.021.

Song, F., and M. N. Toksöz (2011), Full-waveform Based Complete Moment Tensor Inversion and Source Parameter Estimation from Downhole Microseismic Data for Hydrofracture Monitoring, *Geophysics*, *76*(6), WC103, doi:10.1190/GEO2011-0027.1.

St-Onge, A., and D. W. Eaton (2011), Noise Examples from Two Microseismic Datasets, *CSEG Recorder*, *36*(10), 46–49.

Stierle, E., Vavryčuk, V., Šilený, J. and M. Bohnhoff (2014), Resolution of non-double-couple components in the seismic moment tensor using regional networks—I: a synthetic case study, *Geophysical Journal International*, *196*, 1869–1877, doi:10.1093/gji/ggt502.

Sutherland, B. R., and W. R. Peltier (1992), The stability of stratified jets, *Geophys. Astrophys. Fluid Dyn.*, *66*, 101–131, doi:10.1080/03091929208229053.

Sutherland, B. R., and W. R. Peltier (1994), Turbulence transition and internal wave generation in density stratified jets, *Phys. Fluids A*, *6*, 1267–1284, doi:10.1063/1.868295.

Sutherland, B. R. (2006), Rayleigh Wave-Internal Wave Coupling and Internal Wave Generation Above a Model Jet Stream, *J. Atmos. Sci.*, *63*, 1042–1055, doi:10.1175/JAS3658.1.

Smylie, D. E. (2013), *Earth dynamics: deformations and oscillations of the rotating Earth*, Cambridge University Press, Cambridge.

Sun, R., and G. A. McMehan (1988), Finite-Difference Modeling of Borehole Resonances, *Energy Sources*, *10*(1), 55–75, doi:10.1080/00908318808908916.

Tary, J. B., Herrera, R. H., Han, J., and M. van der Baan (2014a), Spectral estimation - What's new? What's next?, *Reviews of Geophysics*, accepted.

Tary, J. B., Herrera, R. H., and M. van der Baan (2014b), Time-Varying Autoregressive Model for Spectral Analysis of Microseismic Experiments and Long-Period Events,

Geophysical Journal International, 196(1), 600–611, doi:10.1093/gji/ggt400.

Tary, J. B., and M. van der Baan (2012), Potential use of resonance frequencies in microseismic interpretation, *The Leading Edge*, 31(11), 1338–1346, doi:10.1190/tle31111338.1.

Tary, J. B., van der Baan, M., and D. W. Eaton (2014c), Interpretation of resonance frequencies recorded during hydraulic fracturing treatments, *Journal of Geophysical Research*, 119, 1295–1315, doi:10.1002/2013JB010904.

van der Baan M., D. Eaton, and M. Dusseault (2013), Microseismic monitoring developments in hydraulic fracture stimulation, in *Effective and sustainable hydraulic fracturing*, edited by R. Jeffrey et al., InTech, 439-466, doi:10.5772/56444.

Vermilye, J. M., and C. H. Scholz (1995), Relation between vein length and aperture, *Journal of Structural Geology*, 17(3), 423–434, doi:10.1016/0191-8141(94)00058-8.

Warpinski, N. (2009), Microseismic Monitoring: Inside and Out, *Journal of Petroleum Technology*, 61(11), 80–85, doi:10.2118/118537-MS.

Zhang, J., Gerstoft, P., Shearer, P. M., Yao, H., Vidale, J. E., Houston, H., and A. Ghosh (2011), Cascadia tremor spectra: Low corner frequencies and earthquake-like high-frequency falloff, *Geochem. Geophys. Geosyst.*, 12, Q10007, doi:10.1029/2011GC003759.

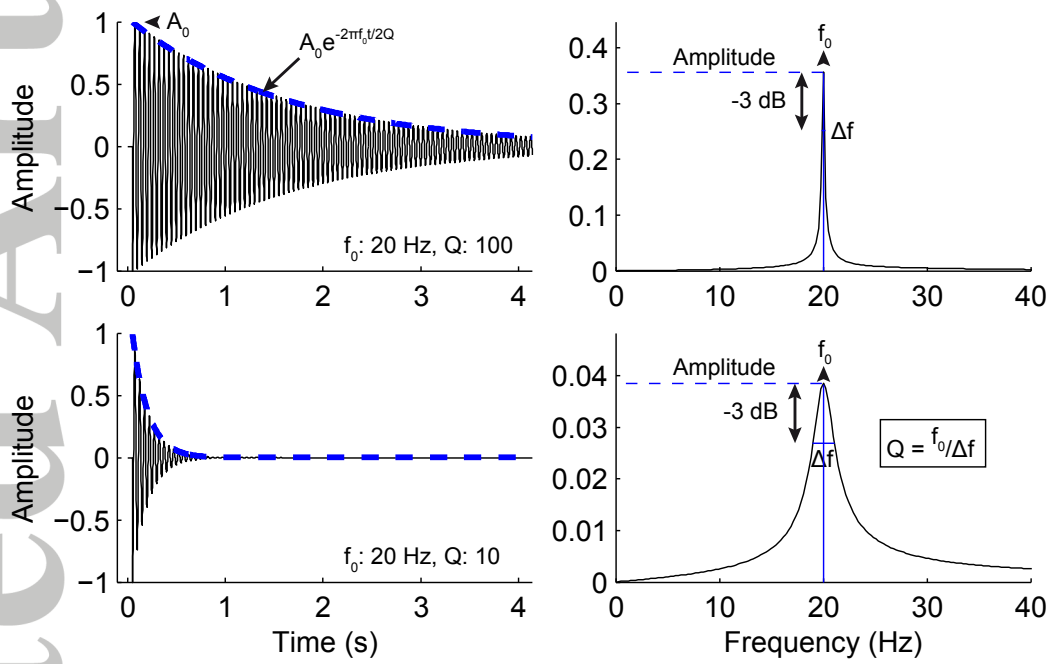


Figure 1. Illustration of the definition of quality factors Q , peak frequency f_0 , frequency bandwidth Δf and amplitude in the Fourier spectra (right) of two waveforms (left).

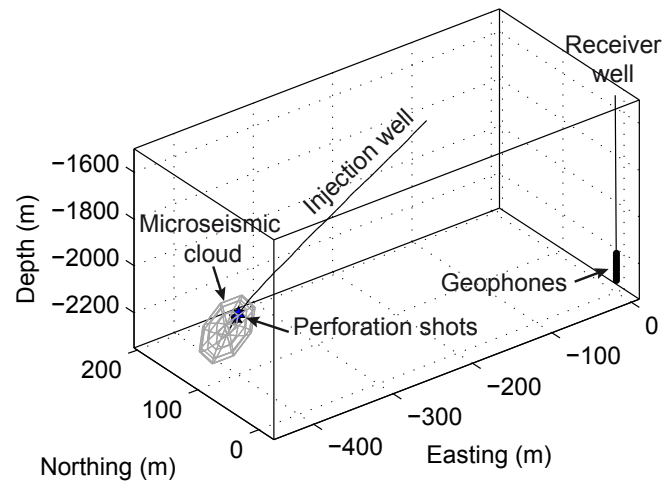


Figure 2. Experimental setup of the microseismic experiment. The two perforation shots are indicated by blue stars and the 12 geophones by black dots. The ellipsoid in gray corresponds to the microseismic cloud showing the locations of the microseismic events recorded during both hydraulic fracturing stages.

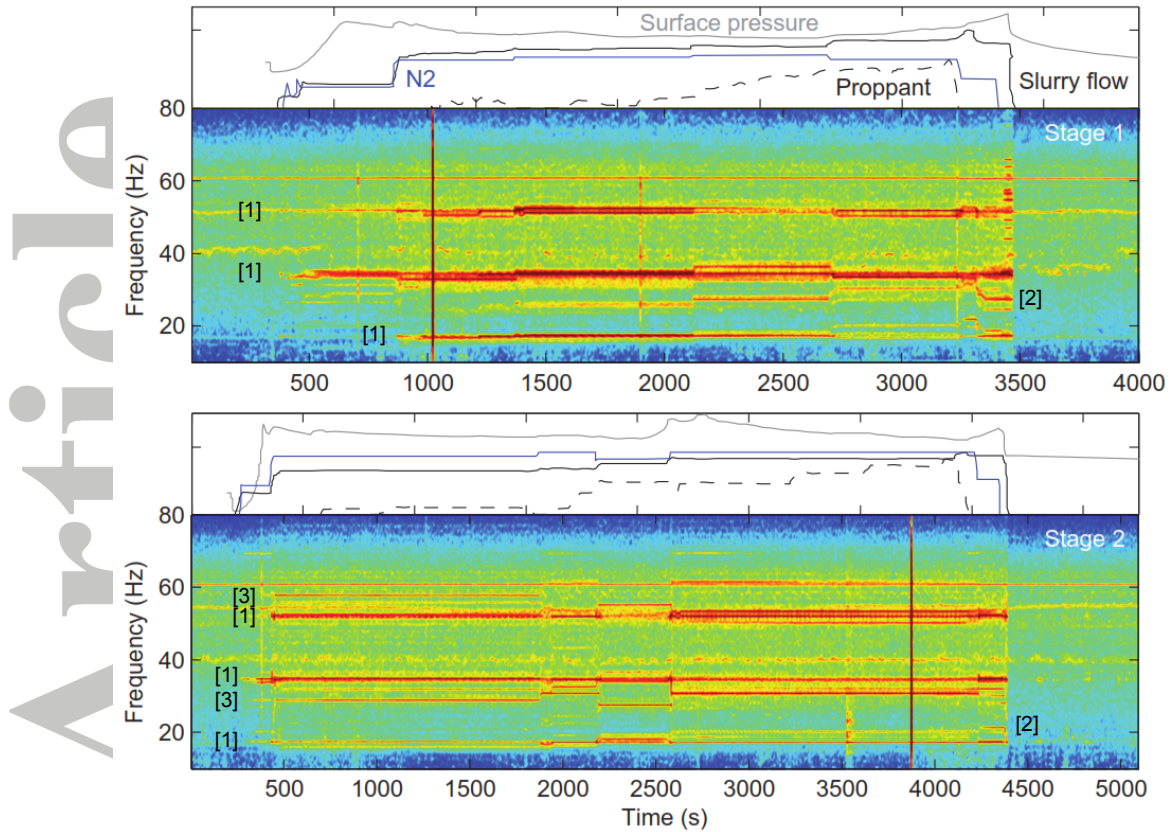


Figure 3. Surface treatment curves and AR time-frequency representation of the two stages of the microseismic experiment (geophone 12, vertical component). The data are downsampled from 4000 Hz to 160 Hz prior to the time-frequency analysis. Hot colors correspond to high amplitudes. A window of 5 s with 90 % overlap, with a filter order of 100 for both stages are used to compute the short-time autoregressive response [Tary *et al.*, 2014b]. Numbers on time-frequency representations indicate the different groups of resonances: main resonance at [1] 17 Hz with overtones at +17 Hz, [2] 27 Hz and 16 Hz with harmonics at +8 Hz, [3] 29 Hz with overtones at +29 Hz (See also Figures 5 and 6). Treatments plots have linear scales and the curves are scaled to fit in the same graph (gray line = surface pressure, black line = slurry flow, blue line = injection rate of nitrogen, and dashed line = proppant concentration). Time shifts are applied to the treatment curves to align them on the time-frequency representations, +323 and +227 s for the first and second stage, respectively.

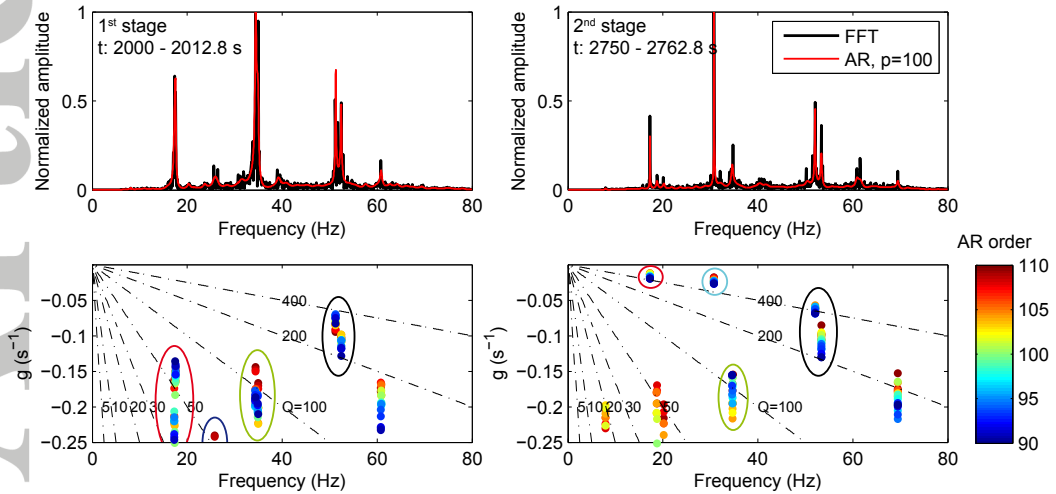


Figure 4. Fourier and AR spectra (top) for two segment of signals, one during the first stage (left) and one during the second stage (right), as well as growth rates ($g = -f/2Q$) estimated from the AR poles as a function of frequency (bottom). The AR spectra are calculated using the optimum AR order p of 100, and the AR poles for Q -factor estimation are computed for AR orders between 90 and 110. On the growth rate vs frequency plot, the color code of the dots indicates the AR order and dashed lines with numbers are lines of constant Q -factors. AR poles corresponding to the main spectral lines are circled using the same color code as Figures 5b and 6b. FFT: Fast Fourier Transform.

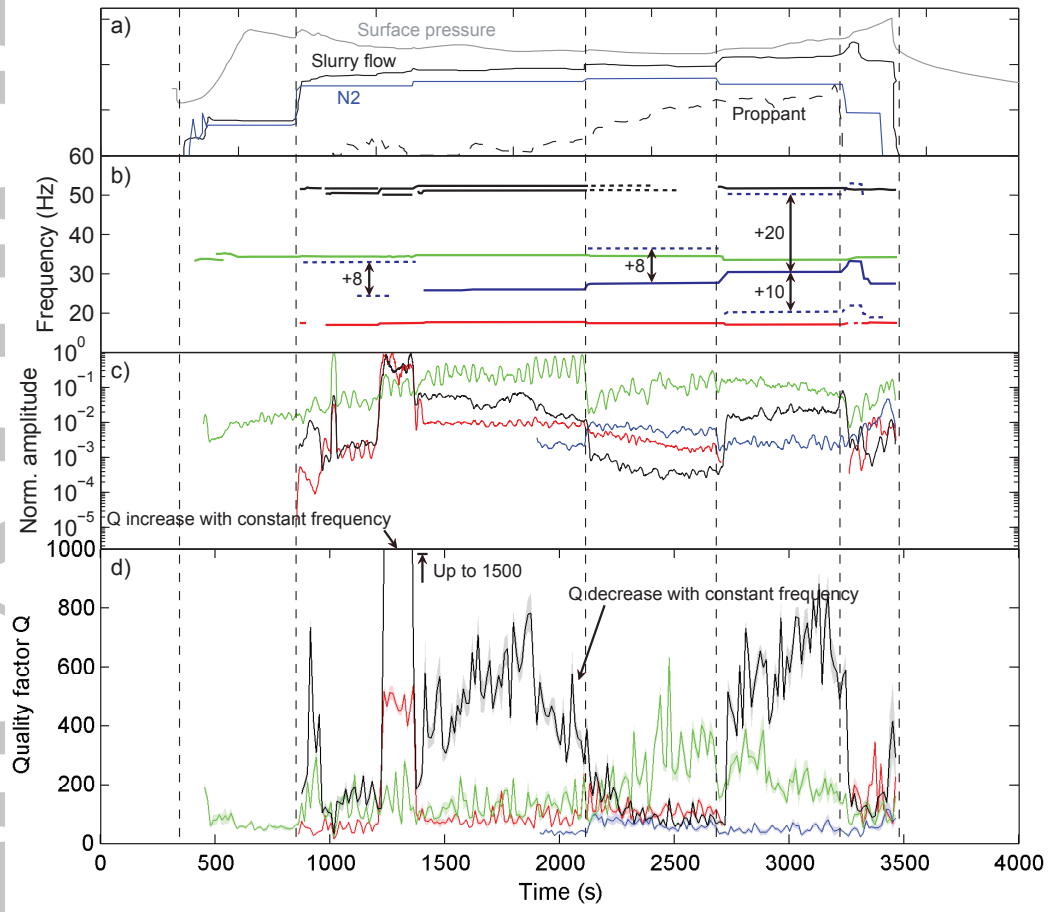


Figure 5. Treatment conditions (a), sketch of the peak frequencies (b), resonance amplitudes (c) and estimates of quality factors Q (d) of the resonances shown in Figure 3 for the first stage of the microseismic experiment. The Q -factors were measured on a sliding window of 12.8 s for AR orders ranging from 90 to 110. The Q -factor mean values and standard deviations for each resonance are shown by the curves and shade areas, respectively. The same color code was used for peak frequencies and Q -factors. No Q factors are shown for resonances whose low amplitudes prevent reliable measurements.

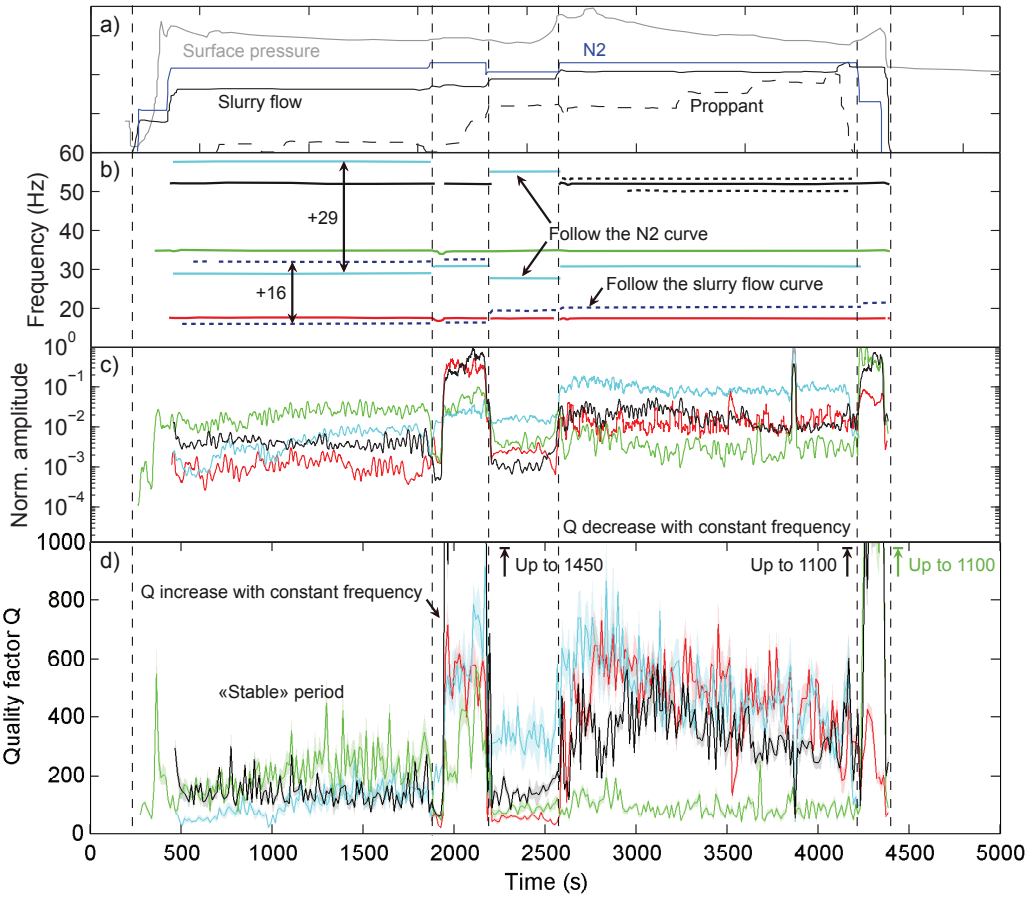


Figure 6. Treatment conditions (a), sketch of the peak frequencies (b), resonance amplitudes (c) and estimates of quality factors Q (d) of the resonances shown in Figure 3 for the second stage of the microseismic experiment. Same procedure as for Figure 5.

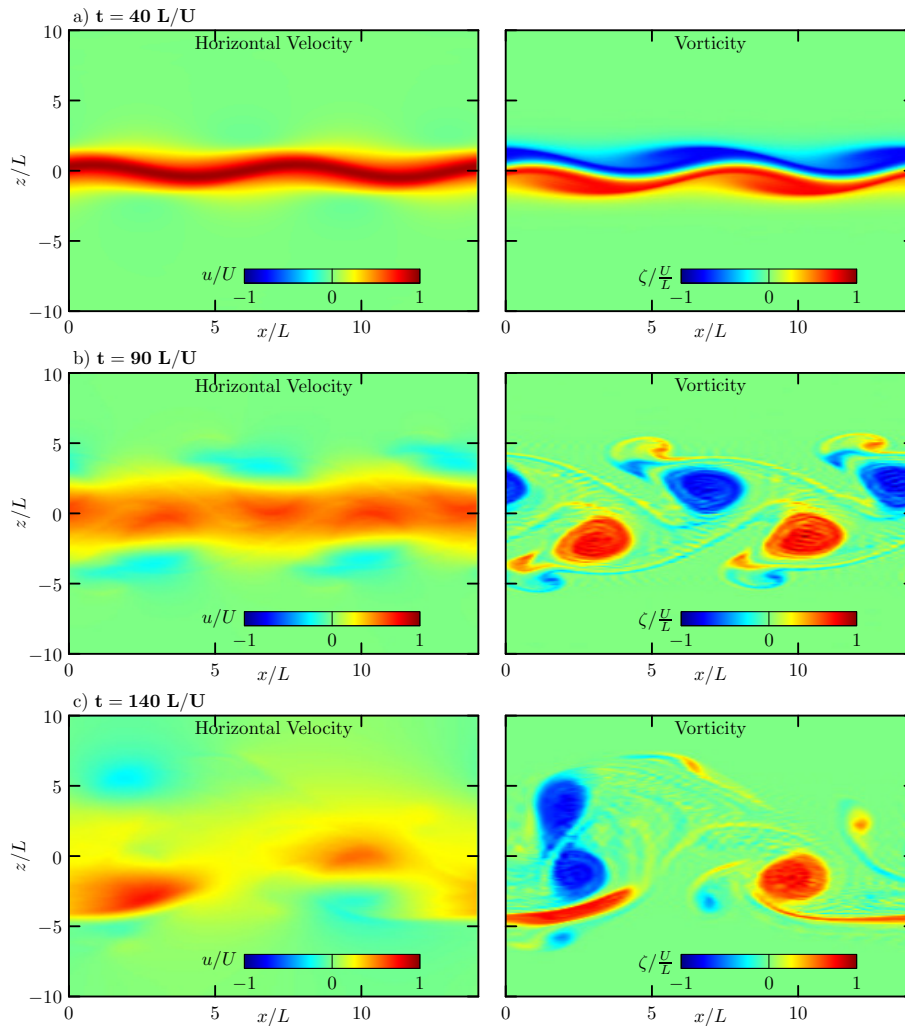


Figure 7. Results from a fully nonlinear numerical simulation of an unstable jet showing snapshots of horizontal velocity u (left) and vorticity ζ (right) at three successive times a) as the instability grows, b) after the jet has broken into two pairs of opposite signed vortices and c) as the vortices merge to form a single vortex pair. This simulation assumes a jet with maximum speed $U = 200$ m/s and half width $L = 0.005$ m. The actual times of the snapshots are 0.001 s apart. The Reynolds number of this flow is $Re = 7400$.